



Title	Technical Note : Range verification of pulsed proton beams from fixed-field alternating gradient accelerator by means of time-of-flight measurement of ionoacoustic waves
Author(s)	Nakamura, Yuta; Takayanagi, Taisuke; Uesaka, Tomoki; Unlu, Mehmet Burcin; Kuriyama, Yasutoshi; Ishi, Yoshihiro; Uesugi, Tomonori; Kobayashi, Masanori; Kudo, Nobuki; Tanaka, Sodai; Umegaki, Kikuo; Tomioka, Satoshi; Matsuura, Taeko
Citation	Medical physics, 48(9), 5490-5500 <a href="https://doi.org/10.1002/mp.15060">https://doi.org/10.1002/mp.15060</a>
Issue Date	2021-09-21
Doc URL	<a href="http://hdl.handle.net/2115/90386">http://hdl.handle.net/2115/90386</a>
Rights	This is the peer reviewed version of the following article: Nakamura, Y, Takayanagi, T, Uesaka, T, et al. Technical Note: Range verification of pulsed proton beams from fixed-field alternating gradient accelerator by means of time-of-flight measurement of ionoacoustic waves. Medical Physics. 2021; 48: 5490– 5500, which has been published in final form at <a href="https://doi.org/10.1002/mp.15060">https://doi.org/10.1002/mp.15060</a> . This article may be used for non-commercial purposes in accordance with Wiley Terms and Conditions for Use of Self-Archived Versions. This article may not be enhanced, enriched or otherwise transformed into a derivative work, without express permission from Wiley or by statutory rights under applicable legislation. Copyright notices must not be removed, obscured or modified. The article must be linked to Wiley 's version of record on Wiley Online Library and any embedding, framing or otherwise making available the article or pages thereof by third parties from platforms, services and websites other than Wiley Online Library must be prohibited.
Type	article (author version)
File Information	Manuscript_MedPhysTechnicalNote_20210624.pdf



[Instructions for use](#)

1           **Technical Note: Range verification of pulsed proton beams from**  
2           **fixed-field alternating-gradient accelerator by means of time-of-flight**  
3           **measurement of ionoacoustic waves**

4  
5   **Running title:** Acoustic range verification of protons from FFA

6  
7   Yuta Nakamura<sup>1,†</sup>, Taisuke Takayanagi<sup>2,3,†</sup>, Tomoki Uesaka<sup>2</sup>, Mehmet Burcin Unlu<sup>4</sup>,  
8   Yasutoshi Kuriyama<sup>5</sup>, Yoshihiro Ishi<sup>5</sup>, Tomonori Uesugi<sup>5</sup>, Masanori Kobayashi<sup>6</sup>, Nobuki Kudo<sup>7</sup>,  
9   Sodai Tanaka<sup>8</sup>, Kikuo Umegaki<sup>8,9</sup>, Satoshi Tomioka<sup>8</sup>, Taeko Matsuura<sup>8,9,\*</sup>

10  
11   <sup>†</sup> Yuta Nakamura and Taisuke Takayanagi contributed equally to this work.

12  
13   **\*Corresponding author:** Dr Taeko Matsuura, Faculty of Engineering, Hokkaido University,  
14   North-15 West-7, Kita-ku, Sapporo, Hokkaido, 060-8638, Japan. Tel: +81-11-706-5254; Email:  
15   matsuura@med.hokudai.ac.jp

16  

---

<sup>1</sup> Graduate School of Engineering, Hokkaido University, North-13 West-8, Kita-ku, Sapporo, Hokkaido, 060-8628, Japan

<sup>2</sup> Graduate School of Biomedical Science and Engineering, Hokkaido University, North-13 West-8, Kita-ku, Sapporo, Hokkaido, 060-8628, Japan

<sup>3</sup> Hitachi Ltd., 1-1 7-chome, Omika-cho, Hitachi-shi, Ibaraki, 319-1292, Japan

<sup>4</sup> Department of Physics, Bogazici University, Bebek, Istanbul, 34342, Turkey

<sup>5</sup> Institute for Integrated Radiation and Nuclear Science, Kyoto University, Osaka, 590-0494, Japan

<sup>6</sup> Planetary Exploration Research Institute, Chiba Institute of Technology, Chiba, 275-0016, Japan

<sup>7</sup> Faculty of Information Science and Technology, Hokkaido University, North-14, West-9, Kita-ku, Sapporo, Hokkaido, 060-0814, Japan

<sup>8</sup> Faculty of Engineering, Hokkaido University, North-13 West-8, Kita-ku, Sapporo, Hokkaido, 060-8628, Japan

<sup>9</sup> Proton Beam Therapy Center, Hokkaido University Hospital, North-15 West-7, Kita-ku, Sapporo, Hokkaido, 060-8638, Japan

17 **Abstract**

18 **Purpose:** Ionoacoustics is one of the promising approaches to verify the beam range in proton  
19 therapy. However, the weakness of the wave signal remains a main hindrance to its application  
20 in clinics. Here we studied the potential use of a fixed-field alternating-gradient accelerator  
21 (FFA), one of the accelerator candidates for future proton therapy. For such end, magnitude of  
22 the pressure wave and range accuracy achieved by the short-pulsed beam of FFA were assessed,  
23 using both simulation and experimental procedure.

24 **Methods:** A 100 MeV proton beam from the FFA was applied on a water phantom, through the  
25 acrylic wall. The beam range measured by the Bragg peak (BP)-ionization chamber (BPC) was  
26 77.6 mm, while the maximum dose at BP was estimated to be 0.35 Gy/pulse. A hydrophone was  
27 placed 20 mm downstream of the BP, and signals were amplified and stored by a digital  
28 oscilloscope, averaged, and low-pass filtered. Time-of-flight (TOF) and two relative TOF values  
29 were analyzed in order to determine the beam range. Furthermore, an acoustic wave transport  
30 simulation was conducted to estimate the amplitude of the pressure waves.

31 **Results:** The range calculated when using two relative TOF was  $78.16 \pm 0.01$  and  $78.14 \pm 0.01$   
32 mm, respectively, both values being coherent with the range measured by the BPC (the  
33 difference was 0.5–0.6 mm). In contrast, utilizing the direct TOF resulted in a range error of 1.8  
34 mm. Five and fifty-fold averaging was required to suppress the range variation to below 1 mm  
35 for TOF and relative TOF measures, respectively. The simulation suggested the magnitude of  
36 pressure wave at the detector exceeded 7 Pascal.

37 **Conclusion:** A submillimeter range accuracy was attained with a pulsed beam of about 21 ns  
38 from an FFA, at a clinical energy using relative TOF. To precisely quantify the range with a  
39 single TOF measurement, subsequent improvement of the measuring system is required.

40

41 **Keywords:** proton therapy, range verification, ionoacoustics

## 42 **1. Introduction**

43 While proton therapy potentially allows better dose conformality compared to photon therapy  
44 because of the Bragg peak (BP), the full potential of the BP is yet to be exploited because of the  
45 range uncertainty.<sup>1</sup> Multiple sources of range uncertainty exist, including the conversion from  
46 the computed tomography (CT) value to stopping power ratio, anatomical changes of the patient,  
47 and organ motion, and much effort has been made to reduce this range uncertainty.<sup>2</sup> In vivo  
48 range verification during or shortly after treatment is a promising approach, and three methods  
49 have been proposed so far, namely prompt gamma detection (PGD),<sup>3</sup> positron emitter  
50 tomography (PET),<sup>4</sup> and ionoacoustics.<sup>5</sup> PGD and PET detect the gamma-ray arising from the  
51 nuclear reaction between protons and nuclei along the beam path. Both are currently used in  
52 clinics<sup>6,7</sup> and should detect the beam range in a few millimeter accuracy.<sup>8</sup>

53 The method using the ionoacoustic range verification is based on acoustic waves arising from  
54 a medium being hit by a pulsed proton/ion beam.<sup>9</sup> Unlike PGD and PET, requiring bulky and  
55 expensive gamma-ray detectors around patients, the acoustic wave detection system comprises a  
56 single or an array of hydrophones, requiring smaller space, and is more affordable.<sup>10</sup> Hayakawa  
57 et al.<sup>11</sup> first applied this method to a patient in which the feasibility of monitoring the proton  
58 dose distributions in patients was suggested by sensing acoustic pulses. Recently, many studies,  
59 both experimental and numerical, have been conducted to exploit the ionoacoustics to reduce  
60 the range uncertainty during proton therapy.<sup>12</sup> The experiments were performed using a  
61 linac,<sup>13,14</sup> a synchrotron,<sup>11,15,16,17</sup> a tandem accelerator,<sup>18</sup> a cyclotron,<sup>19</sup> a laser-plasma  
62 accelerator,<sup>20</sup> a hospital-based isochronous cyclotron,<sup>21,22</sup> and a synchrocyclotron,<sup>23,24</sup> all with  
63 positive results. Specifically, clinically relevant energy beams were used by Jones et al. (190  
64 MeV and 230 MeV beams, accelerated by a clinical cyclotron)<sup>21,22</sup> and by Lehrack et al. and  
65 Patch et al. (energy between 145 MeV and 227 MeV, and energy  $\geq$  125 MeV, respectively, from  
66 a clinical synchrocyclotron).<sup>23,24</sup>

67 Although these results substantiate the usefulness of ionoacoustics, its clinical application has

68 been hampered by the faint signal amplitude attainable hitherto. Pressure waves are generated  
69 efficiently in case thermal and stress confinement conditions are met, which is accomplished  
70 when pulse duration is no more than  $5 \mu\text{s}$ <sup>23</sup> besides what signal amplitude is further increased if  
71 the pulse duration is shortened. Jones et al. modulated a clinical cyclotron ion source current to  
72 generate pulses of  $17 \mu\text{s}$ , which are shorter than standard treatment delivery. However, in their  
73 work the wave amplitude obtained was limited to 25 mPa or below, at a maximum instantaneous  
74 beam current of 790 nA, with  $11.5 \times 10^7$  protons, which entailed an averaging of 1024-fold.<sup>22</sup>  
75 Even with a superconducting synchrocyclotron, which achieved the shortest pulse among  
76 therapy machines ( $3.7 \mu\text{s}$ ), Lehrack et al. reported that a dose of 10 Gy (2 pC per pulse  $\times 1000$   
77 average) was required to reach submillimeter range accuracy.<sup>23</sup> Recently, with the same  
78 accelerator, Patch et al. demonstrated that the range verification is possible with the clinical  
79 dosage of 0.5 Gy, however, the customized fine-tuned detectors and amplifiers were required,  
80 which are not available commercially.<sup>24</sup> On the other hand, non-clinical machines such as  
81 tandem accelerator,<sup>18</sup> linac,<sup>14</sup> and laser-plasma accelerator<sup>20</sup> produce the shortest pulses of 8 ns,  
82 250 ns, and 30 fs, respectively. In the last two instances, range measurement was done with a  
83 single<sup>20</sup> or 128-fold averaging,<sup>14</sup> conversely the beam energies with all accelerators being far  
84 below those that characterize therapeutic proton beams.

85 In the present study, we explored ionoacoustic range detection using a short-pulsed proton  
86 beam from an FFA.<sup>25,26,27</sup> The beam properties were within the range of that of clinical  
87 conditions [100 MeV,  $1.12 \times 10^8$  proton/pulse (0.35 Gy at BP), lateral beam size  $\sim 5$  mm], yet  
88 notably the pulse width was much smaller than that in clinical contexts ( $\sigma \sim 21$  ns). Here we  
89 estimate the beam range by measuring the time-of-flight (TOF) of the direct wave emitted from  
90 the BP (referred to as  $\gamma$ -wave), as well as of the differences of TOF (referred to as relative TOF)  
91 between direct wave and the ones reflected at the phantom wall. Relative TOF was also used in  
92 prior studies<sup>14,18,19</sup> and has the considerable advantage of not being affected neither by the  
93 hydrophone positioning error nor the signal delay. The accuracy of the TOF methods was

94 assessed in comparison with the range detected by the dose measurement by the BPC. Moreover,  
95 an acoustic wave transport simulation was performed to obtain the absolute amplitude of the  
96 pressure waves.  
97

## 98 2. Materials and Methods

### 99 2.1 Proton beam from the FFA

100 The 100 MeV proton beam accelerated by the FFA at Kyoto University<sup>28,29</sup> was extracted at a  
101 repetition rate of 30 Hz and incident on the DigiPhant PT water phantom (IBA Dosimetry,  
102 Schwarzenbruck, Germany) through an acrylic wall of 1 cm. FFA designed for proton therapy  
103 could in principle accelerate protons up to 250 MeV<sup>25</sup> or 350 MeV<sup>26</sup> but only representative  
104 energy was used in this study. The pulse width was estimated at  $\sim 21$  ns ( $1\sigma$ ) according to the  
105 measurement using an EJ-200 plastic scintillator placed at the exit of the vacuum beam duct  
106 (Figure 1(B)). The scintillator coupled to a photomultiplier tube indirectly measures the beam  
107 pulse shape by detecting mainly the loss protons and gamma-ray emitted by nuclei activated by  
108 proton irradiation. The number of particles per pulse was measured using the Faraday cup and  
109 estimated as  $(1.17 \pm 0.06) \times 10^8$ , which is comparable to one pulse in a clinical setting.<sup>30</sup> The  
110 corresponding peak current was 0.4 mA.

111

### 112 2.2 Measurement of dose profiles

113 The Bragg curve shape was acquired by scanning the BPC (PTW34070, Freiburg, Germany)  
114 along the beam axis (Figure 2a). Beam range was defined at the BP maximum and estimated as  
115  $R_{BPC} = 77.6$  mm (mean of the two independent experiments). A transmission monitor Type  
116 34014 (PTW, Freiburg, Germany) was used as the reference monitor. The lateral beam profile  
117 was obtained using a radiochromic film EBT3 attached to the surface of the water phantom  
118 (Figure 2b, c). The Satera MF8570Cdw (Canon Ltd.) was used as the film scanner, and at the  
119 surface of the water phantom, the respective beam size ( $1\sigma$ ) was 4.7 mm, vertically, and 5.7 mm,  
120 horizontally.

121

### 122 2.3 Acoustic wave measurement

123 The unfocused type immersion hydrophone (V391-SU, Olympus, Waltham, USA) with a

124 central frequency of 0.5 MHz was placed 20 mm downstream of the range measured by the  
125 BPC in the water phantom. The hydrophone was positioned by aligning the detector surface to  
126 the lasers mounted on the room walls. The sensitive volume is assumed to be located at the  
127 detector surface. The water employed was deionized and degassed, with its temperature  
128 maintained at 22°C throughout the experiment, corresponding to sound speed of 1488.4 m/s. As  
129 described later, the frequency spectrum of the acoustic waves originating from the BP has its  
130 maximum at around 100 kHz. On the other hand, the peak and upper/lower -6 dB frequencies of  
131 the hydrophone were 0.48, 0.63, and 0.33 MHz, respectively, according to the datasheet  
132 provided by the manufacturer. A control signal of the beam extraction kicker of the FFA was  
133 used for triggering data acquisition, and time zero was defined at the peak of the scintillator  
134 signal. Signals were amplified using a 46 dB amplifier (SA230-F5, NF Corporation, Japan),  
135 with a flat frequency response over the bandwidth of 1 kHz~100 MHz (+0.5, -3 dB), and then  
136 stored through digital oscilloscope at a 50 MS/s sampling rate, after averaging 5–50 events. A  
137 low-pass filter with a cutoff frequency of 1 MHz was used for filtering the RF noise at 8 MHz.  
138 We investigate whether the result depends on the incident beam energy by setting additional  
139 acrylic plates of various thicknesses (4 mm–20 mm) in front of the water phantom and repeated  
140 the measurement.

141

#### 142 2.4 TOF and relative TOF metrics

143 In the previous research, beam range estimation has predominantly relied on the absolute  
144 TOF of the compression peak of the  $\gamma$ -wave. Here, beyond the conventional TOF of direct  
145  $\gamma$ -waves (wavelet (a) in Figure 3), we explored the relative TOF metrics,<sup>14,18,19</sup> in order to avoid  
146 the bias of hydrophone positioning error (the difference between the TOF of wavelets (a) and (c)  
147 or (d) in Figure 3). Denoting the acoustic arrival time of each wavelet as  $\tau^{(i)}$  ( $i = a, c, d$ ), the  
148 beam range ( $R$ ) is estimated by

$$149 \quad R = L_1 + L_2 + S_{\text{acryl}}L_{\text{wall}} - c_w \tau^{(a)},$$



150 when using the conventional TOF method, or by the expression

151 
$$R = c_w \left( \frac{\tau^{(c)} - \tau^{(a)}}{2} \right) + S_{\text{acryl}} L_{\text{wall}} \text{ or } R = c_w \left\{ \left( \frac{\tau^{(d)} - \tau^{(a)}}{2} \right) - \frac{L_{\text{wall}}}{c_a} \right\} + S_{\text{acryl}} L_{\text{wall}},$$

152 if addressing relative TOF metrics.  $L_1$ ,  $L_2$ , and  $L_{\text{wall}}$  are, respectively, the distances from the  
153 wall to the BP, and from the BP to the detector position, and the acrylic wall thickness.  $S_{\text{acryl}}$   
154 represents the relative stopping power of acryl (= 1.16), while  $c_w$  and  $c_a$  are the sound speed  
155 in water and acryl, respectively.

156

## 157 2.5 Acoustic wave simulation

158 The waveform obtained from the experiment was further explored by conducting an acoustic  
159 wave simulation using a simple point-like detector with a constant frequency response and no  
160 delay. The thermoacoustic wave emission and transport equation, from the energy deposition of  
161 proton pulse, is described by the following expression,

162 
$$\frac{1}{v^2} \frac{\partial^2 p}{\partial t^2} - \nabla^2 p = (\Gamma/v^2) E(\vec{r}) I'(t),$$

163 where  $E(\vec{r})$  corresponds to the distribution of transferred energy density [ $\text{J}/\text{m}^3$ ].  $I'(t)$  is the  
164 time derivative of the normalized beam current [ $1/\text{s}$ ], with the time integral of  $I(t)$  over  $-\infty <$   
165  $t < \infty$  having been normalized to 1, and  $\Gamma$  and  $v$  are the dimensionless Gruneisen  
166 coefficient and the sound velocity [ $\text{m}/\text{s}$ ] of the medium, respectively.<sup>31</sup> In this simulation, we  
167 used the k-WAVE Matlab toolbox<sup>32</sup>, which solves the coupled first-order differential equations  
168 for the acoustic particle velocity and density, rather than the above equivalent second-order  
169 equation. The acoustic properties of the water and acryl used as the simulation input was  
170 summarized in Table 1. Geant4 Monte Carlo code (ver.9.3)<sup>33</sup> was used to obtain  $E(\vec{r})$ , where  
171 the input beam parameters, including the mean energy of the incident protons, energy spread,  
172 and beam size were tuned to reproduce the measured Bragg curve and lateral beam profiles. For  
173 simplicity, protons were assumed to have momenta parallel to the beam axis at the phantom wall.  
174 The beam range, defined at the BP maximum, was  $R_{\text{sim}} = 76.3$  mm, and the same number of

175 protons per pulse and the detector position as the experiment were used in the simulation. The  
176 time-varying source was used in the k-WAVE simulation with the Gaussian pulse structure with  
177 a sufficiently small width (250 ns ( $1\sigma$ )). A perfectly matched layer is applied to the boundary,  
178 absorbing all outgoing acoustic waves and preventing reflection. The calculation was performed  
179 in 3D with a grid of  $0.3 \times 0.3 \times 0.3$  mm<sup>3</sup>. The time-step was set to 5 ns to ensure stability  
180 (Courant–Friedrichs–Lewy number  $< 1$ ). Due to the limited computational memory capacity, the  
181 calculation volume was set as  $50 \times 50 \times 100$  mm<sup>3</sup>.

182

183

184 **3. Results**

185 3.1 Range estimation from measured acoustic waveform

186 Figure 4 shows the observed acoustic waveform without additional acrylic plates in front of  
187 the phantom, averaged over 50 measurements. The signal observed around time zero was the  
188 electromagnetic noise emitted from the beam extraction kicker of the FFA. As explained below,  
189 the hydrophone detected the four wavelets demonstrated in Figure 3.

190 Wavelet (a) shows the  $\gamma$ -wave from the BP. The arrival times of positive and negative peaks  
191 were 13.9 and 15.3  $\mu\text{s}$ , denoted as  $\tau_p^{(a)}$  and  $\tau_n^{(a)}$ , respectively. Because the pulse width of the  
192 FFA (FWHM of  $\sim 50$  ns) is smaller than the size of BP divided by the sound speed (FWHM of  
193 5.7  $\mu\text{s}$ ) by three orders of magnitude, the wavelet size (peak-to-peak distance of 1.4  $\mu\text{s}$ ), is  
194 determined by the shape of the Bragg curve. The positive peak is higher than the negative peak,  
195 reflecting a higher dose gradient of the distal portion of the BP compared to the proximal  
196 portion.

197 Wavelet (c) and (d) are the  $\gamma$ -waves reflected at the water-acrylic wall and acrylic wall-air  
198 boundary, respectively. Taking into account the order of acoustic impedance (acryl > water >  
199 air) (Table 1), phase shift is  $0^\circ$  and  $180^\circ$  on reflection, respectively. As shown in the Appendix A,  
200 in theory, the reflected waves and direct wave are related by  $p_{\text{reflected}}(t) \propto -\lambda p_{\text{direct}}(-t +$   
201  $\Delta t)$  where  $\lambda$  and  $\Delta t$  indicate the phase shift and the distance from the detector to its mirrored  
202 image reflected at the interface. The  $\lambda$  and  $\Delta t$  are +1 and  $\frac{2(L_1+L_2)}{c_w}$  for wavelet (c) and -1 and  
203  $\frac{2(L_1+L_2)}{c_w} + \frac{2L_{\text{wall}}}{c_a}$  for wavelet (d), respectively. The negative peak, in the case of wavelet (c),  
204 arrived at 104.5  $\mu\text{s}$  (denoted by  $\tau_n^{(c)}$ ), and was superior to the positive one for the same reason  
205 specified above. Similarly, in the case of wavelet (d), the positive peak is higher than the  
206 negative peak and it arrives at 111.6  $\mu\text{s}$ , symbolized by  $\tau_p^{(d)}$ .

207 Finally, wavelet (b) is the resonance wave generated in the acrylic wall. Because both water  
208 and air have a lower acoustic impedance than acryl, nodes occur at both ends. We did not use

209 this wavelet for relative TOF, because the acoustic source of the resonance wave has a finite size  
210 and we did not have a clear idea which point in the wall can be regarded as the wave origin.  
211 Meanwhile, the resonance frequency was used to derive the sound speed of acryl in the  
212 experiment.

213 Figure 5A shows the frequency spectrum of the waveform in Figure 4. The sampled data over  
214 a time interval between 0  $\mu\text{s}$  and 120  $\mu\text{s}$  were Fourier transformed. The peaks at 0.12, 0.43, and  
215 0.72 MHz originated from the resonance wave (b). The periodic dips on the spectrum are  
216 because of the repeated arrival of the  $\gamma$ -waves ((a), (c), and (d)).<sup>34</sup> To extract the spectrum of  
217 wavelet (a) (the time interval of  $5 \mu\text{s} \leq t < 50 \mu\text{s}$ ) and wavelets (c) and (d) ( $100 \mu\text{s} \leq t < 120 \mu\text{s}$ ),  
218 data out of these intervals were set to zero and zero-padding was applied until  $t < 1,311 \mu\text{s}$   
219 before Fourier transformation (Figure 5B). The figure suggests that both frequencies of the  
220 direct and reflected  $\gamma$ -waves were concentrated below 0.6 MHz, with the maximum reached at  
221  $\sim 60$  kHz or  $\sim 340$  kHz, respectively.

222 The upper row of Table 2 summarizes the relative TOF between (a) and (c) and between (a)  
223 and (d) and the estimated beam ranges. Negative peak maxima were selected for (a) and (c),  
224 whereas positive peak maximum was selected for (d), since, if the BP shape was symmetric  
225 along the beam line, such as Gaussian assumed in ref.<sup>30</sup>, it should give the correct beam range.  
226 In addition, the smaller peaks of the reflected wavelets (positive peak in (c) and negative peak  
227 (d)) are challenging to address. Comparing these values with the range estimated by the BPC,  
228 the estimation error of two metrics  $\tau_n^{(c)} - \tau_n^{(a)}$  and  $\tau_p^{(d)} - \tau_n^{(a)}$  were both 0.6 mm. As a comparison,  
229 TOF and beam range calculated from the positive peak maximum of wavelet (a) were shown  
230 together, showing that the range error amounts to 1.8 mm with this metric.

231 Table 3 shows the water equivalent thickness (WEL) of the acrylic plates (actual thickness  $\times$   
232 1.16) and the shift of the BP positions estimated from the change in the two metrics  $\tau_n^{(c)} - \tau_n^{(a)}$   
233 and  $\tau_p^{(d)} - \tau_n^{(a)}$  from those without additional acrylic plates, respectively. The data show that the

234 metrics can predict the BP position shift with a  $<0.2$  mm accuracy.

235

### 236 3.2 Acoustic simulation

237 Finally, the red curves in Figure 4 represent the simulated acoustic waveform. The four  
238 wavelets observed in the experiment were observed in the simulation and the maximum  
239 pressure of about 7.5 Pa was reached. The lower row of Table 2 summarizes the TOF and range  
240 values calculated from the three metrics. Comparing these values with the range of the 100 MeV  
241 protons used as the input of the simulation ( $R_{sim} = 76.3$  mm), the estimation errors of all metrics  
242 were within 1 mm.

243 The red curves in Figure 5 show the frequency spectrum of the wavelet (a) and wavelets (c)  
244 and (d) together. The spectrum shows that both the frequencies of the direct and reflected  
245  $\gamma$ -waves were concentrated below 0.5 MHz, with the maximum reached at  $\sim 80$  kHz or  $\sim 50$  kHz,  
246 respectively.

247

## 248 4. Discussion

249 FFA is emerging as one of the accelerator candidates for upcoming proton therapy. This can  
250 achieve high beam intensities and stop acceleration when the required energy has been reached,  
251 permitting extraction at arbitrary energies. We have established that, with its short pulse  
252 duration, the ionoacoustic pressure amplitude reaches approximately 7.5 Pa at 2 cm distal to the  
253 BP, per 0.35 Gy dose at BP. In the meantime, the preceding research that exploited the proton  
254 energies greater than or equal to 50 MeV stated their pulse width as 2–17  $\mu$ s, with the highest  
255 amplitude achieved per 2 Gy dose being 11 Pa, at 6.5 mm distal to the BP (Table 4).<sup>19,22,23,35</sup> This  
256 indicates that, at the same distance from the BP, the short pulse of FFA (20 ns) has the potential  
257 to yield a pressure of about 2–100 times that with the  $\mu$ s pulse, which gives an advantage to the  
258 FFA compared with other clinical machines (See the second right column in Table 4). Note that  
259 the large pressure generated by the cyclotron in ref<sup>19</sup> is partly due to the large Gy/pulse. If the

260 BP dose is normalized to 1 Gy, the pressure yielded by the FFA may be comparable to the  
261 synchrocyclotron, as shown in the rightmost column in Table 4.<sup>23</sup>

262 With the hydrophone used in this experiment, we could not validate the absolute pressure  
263 amplitude of the k-WAVE simulation since it does not have the pressure–voltage conversion  
264 constant. The k-WAVE simulation will have to be validated by a detector cross-calibrated with a  
265 reference transfer standard hydrophone in the future measurement. In a meantime, in a different  
266 experimental setting,<sup>36</sup> we showed that the k-WAVE simulation and the measured waveforms  
267 generated from FFA are similar but an absolute difference in the pressure amplitude was  
268 observed. The reduction of the difference between these waveforms may be possible by  
269 including detailed information about the structure and composition material of the hydrophone  
270 in the simulation, and thus further improvements in the accuracy of the simulation will be  
271 required.

272 In the current work, we applied the absolute and relative TOF metrics for range assessment,  
273 among which the former exploits the direct wave, and the signal amplitude is relatively larger  
274 than the reflection wave. Table 5 comprehends the maximum detected range variation amid 100  
275 measurements and was given by several averages (each measurement consists of 1, 5, 10, and  
276 50 events).<sup>23</sup> Regarding absolute TOF, the range variation was suppressed to 1 mm, even with a  
277 five-fold averaging. Nevertheless, it is subject to a detector-positioning error, as well as  
278 systematic errors prompted by the frequency-dependent delay of the hydrophone, which resulted  
279 in the range estimation error of 1.8 mm. Relative TOF is not impacted by these errors, and  
280 submillimeter range accuracy was achieved with this metric. However, since it uses the  
281 reflection wave, 50-fold averaging was required (Table 5). As Patch et al has denoted in their  
282 recent research, acoustic hardware fine-adjusted to the thermoacoustic emissions (around 100  
283 kHz in case of the  $\gamma$  waves of this study) may be indispensable to achieve the range detection  
284 without averaging, and it is a subject we will address in further investigation.<sup>24</sup>

285 As in a preliminary study, we used a single element hydrophone, while Patch et al. explored a

286 clinical transducer array to acquire a standard ultrasound image of the underlying anatomy, just  
287 before proton beam delivery. Their approach solves the above-stated issue of hydrophone  
288 positioning-derived error, by co-registering the BP and the underlying anatomy images. In  
289 addition, array transducers may be used to estimate the *in vivo* sound speed for the liver<sup>37</sup> and  
290 breast,<sup>38</sup> increasing the accuracy of *in vivo* range verification. Methods that utilize multiple  
291 hydrophones simultaneously to reconstruct the dose distribution were also explored in  
292 simulation study, using 3D filtered backprojection,<sup>39</sup> time-reversal algorithms,<sup>40</sup> and dictionary  
293 method.<sup>41</sup> Such lines of approach may be more suitable for heterogeneous tissues in clinical  
294 settings.

295 The simulation results with an ideal point detector shown in Table 2 indicate that the  
296 submillimeter range estimation error persists with the relative TOF metrics. The deviation of the  
297 range determined by  $\tau_n^{(c)} - \tau_n^{(a)}$  or  $\tau_p^{(d)} - \tau_n^{(a)}$  from the range used as the simulation input was 0.8  
298 mm, reflecting the asymmetry of the Bragg curve along the beam path and is inherent to the  
299 beam shape. If the dissimilarity in the dose gradient of proximal and distal portions of the BP is  
300 minimized, which could be achieved by using the ripple filter to broaden the distal fall-off,<sup>42</sup> the  
301 accuracy of range estimation could be improved. On the other hand, the range error of 0.3 mm  
302 with the absolute TOF method could be due to definition of time zero and the acoustic wave  
303 arrival time. Even though this study made use of the compression peak of the  $\gamma$ -wave to  
304 characterize the arrival time of the direct  $\gamma$ -wave, as was done beforehand,<sup>21,22,23</sup> it does not  
305 necessarily lead to the correct TOF, as underlined by Jones et al.<sup>22</sup> and the analytical method.<sup>43</sup>  
306 Consequently, fine adjustment might be crucial to eliminate this systematic error.

307

## 308 **5. Conclusion**

309 The short-pulsed proton beams from FFA could generate large ionoacoustic waves at  
310 clinically relevant beam energy. Only five-fold averaging was required to suppress the range  
311 deviation to less than 1 mm for absolute TOF, yet the precision was restricted by systematic

312 error arising from the detector positioning and signal delay. In contrast, the range determined  
313 using the relative TOF metrics was in agreement with the value calculated from the depth-dose  
314 measurement to better than 1 mm, but 50-fold averaging was essential, with the detection  
315 system employed in our work. This drawback may be untangled by resorting to fine-tuned  
316 detectors and amplifiers, which will be investigated in the future.

317

### 318 **Acknowledgments**

319 We wish to thank Dr. Hiroki Tanaka, Mr. Masayuki Fujii, Dr. Naoki Miyamoto, and Dr. Seishin  
320 Takao for their valuable support. This research was supported by JSPS KAKENHI Grant No.  
321 21H02859 and JST FOREST Program (Grant Number JPMJFR200X, Japan)..

322

### 323 **Competing Interests**

324 We disclose conflict of interest as following; Authors Taisuke Takayanagi is paid from Hitachi, Ltd.,  
325 Tokyo, Japan. Other authors have no conflict of interest.

326

### 327 **Appendix A.**

328 As described in the main text, the reflected  $\gamma$ -wave (wavelets (c) and (d) in Figures 4) is  
329 approximately obtained by applying time-reversal and sign inversion operations to the direct  
330  $\gamma$ -wave (wavelet (a) in Figures 4) up to a scale factor. In this appendix, this relation is derived  
331 using a simplified model in which the BP is assumed as a one-dimensional finite length heat  
332 source lying on the  $z$ -axis (spreading over a range of  $R_2 < z < R_1$ , where  $0 < R_2 < R_1$ , as  
333 shown in Figure 6(a)).

334 As denoted in Sec. 2.5, the acoustic source term was expressed as  $(\Gamma/v^2)E(\vec{r})I'(t)$ . If the  
335 Gaussian pulse structure of the proton beam is assumed,  $I'(t)$  is anti-symmetric under the  
336 time-reversal operation:  $I'(t) = -I'(-t)$ . In the following, the energy distribution of BP  $E(\vec{r})$   
337 is approximated as  $E(z)\delta(x)\delta(y)$ , where  $\delta(x)$  is the Dirac delta function and  $E(z)$  has finite



338 support over  $R_2 < z < R_1$ . First, if we consider an infinite homogeneous water medium and  
 339 solve the wave equation using the Green's function approach,<sup>24</sup> the pressure wave is expressed  
 340 as

$$341 \quad p(t, z) = \int_{-\infty}^t dt' \int_{R_2}^{R_1} dz' G(z, t; z', t') E(z') (\Gamma/v^2) I'(t') \quad (1)$$

342 where  $G(z, t; z', t')$  is the Green's function satisfying the wave equation in three-dimensional  
 343 free space

$$344 \quad G(z, t; z', t') = \frac{\delta(t - t' - \frac{|z-z'|}{c_w})}{4\pi|z - z'|}$$

345 and  $c_w$  is the sound speed in water. In the following, the detectors are assumed to be positioned  
 346 at  $z_1$  and  $z_2$ , satisfying  $z_1 \gg \bar{R} + \Delta R$  and  $z_2 \ll \bar{R} - \Delta R$ , respectively, where  $\bar{R} \equiv$   
 347  $(R_1 + R_2)/2$  and  $\Delta R \equiv R_1 - R_2$ . Here, the denominator of the Green's function in the  
 348 integrand could be approximated as  $z_1 - \bar{R}$  and  $|z_2 - \bar{R}|$ , respectively, and Eq (1) reduces to

$$349 \quad p_+(t, z_1) \sim \frac{1}{4\pi(z_1 - \bar{R})} \int_{R_2}^{R_1} dz' E(z') (\Gamma/v^2) I\left(t - \frac{z_1 - z'}{c_w}\right)$$

350 and

$$351 \quad p_-(t, z_2) \sim \frac{1}{4\pi|z_2 - \bar{R}|} \int_{R_2}^{R_1} dz' E(z') (\Gamma/v^2) I\left(t - \frac{z' - z_2}{c_w}\right),$$

352 at  $z_1$  and  $z_2$ , respectively. The subscript  $\pm$  indicates the wave propagating toward the positive  
 353 and negative  $z$  direction, respectively. By using  $I'(t) = -I'(-t)$ , we obtain the relation  
 354 between  $p_+(t, z_1)$  and  $p_-(t, z_2)$  as

$$355 \quad p_-(t, z_2) = -\xi \eta p_+(-t + \Delta t, z_1) \quad (2)$$

356 where  $\xi$  expresses the products of transmission ( $T$ ) and reflection ( $R$ ) coefficients at the  
 357 interface of the heterogeneous media and is 1 in this case.  $\eta = \frac{z_1 - \bar{R}}{|z_2 - \bar{R}|}$  is the geometrical factor  
 358 and  $\Delta t = \frac{z_1 - z_2}{c_w}$  is the acoustic wave propagation time between two detectors, indicating that

359 with some simplifications, waves propagating in the positive and negative directions are related

360 to the time-reversal and sign conversion up to a scale factor.

361 Next, we consider the geometry where the layers of air, acrylic wall, and water are stacked next  
362 to each other (Figure 6(b)). Here, Eq. (2) holds as follows. Because no phase change occurs at  
363 the acrylic wall-water boundary for wavelet (c),  $\xi$  is positive in Eq. (2), and  $\xi$  and  $\Delta t$   
364 are  $\xi = R_{\text{acryl-water}}$  and  $\Delta t = \frac{2(L_1+L_2)}{c_w}$ , respectively. However, for wavelet (d), the phase is  
365 shifted by  $180^\circ$  on reflection; hence,  $\xi$  becomes negative. In this case,  $\xi$  and  $\Delta t$  are  $\xi =$   
366  $-(T_{\text{acryl-water}})^2 R_{\text{acryl-air}}$  and  $\Delta t = \frac{2(L_1+L_2)}{c_w} + \frac{2L_{\text{wall}}}{c_a}$ , respectively.

367

### 368 **Data availability**

369 Data that support the findings of this study are available from the corresponding author upon  
370 reasonable request.

371

### 372 **References**

- 373 1. Paganetti H. Range uncertainties in proton therapy and the role of Monte Carlo simulations. *Phys*  
374 *Med Biol.* 2012;57(11):R99-R117.
- 375 2. Yang M, Zhu XR, Park PC et al. Comprehensive analysis of proton range uncertainties related to  
376 patient stopping-power-ratio estimation using the stoichiometric calibration. *Phys Med Biol.*  
377 2012;57(13):4095-4115.
- 378 3. Krimmer J, Dauvergne D, Létang JM, Testa É. Prompt-gamma monitoring in hadron therapy: a  
379 review. *Nucl Instrum Methods Phys Res A.* 2018;878:58-73.
- 380 4. Knopf AC, Lomax A. In vivo proton range verification: a review. *Phys Med Biol.*  
381 2013;58(15):R131-R160.
- 382 5. Hickling S, Xiang L, Jones KC, et al. Ionizing radiation-induced acoustics for radiotherapy and  
383 diagnostic radiology applications. *Med Phys.* 2018;45(7):e707-e721.
- 384 6. Richter C, Pausch G, Barczyk S, et al. First clinical application of a prompt gamma based in vivo  
385 proton range verification system. *Radiother Oncol.* 2016;118(2):232-237.

- 386 7. Nishio T, Miyatake A, Ogino T, Nakagawa K, Saijo N, Esumi H. The development and clinical use  
387 of a beam ON-LINE PET system mounted on a rotating gantry port in proton therapy. *Int J Radiat*  
388 *Oncol Biol Phys* *Biology Physics* 76.1. 2010;76(1):277-286.
- 389 8. Parodi K. Latest developments in-vivo imaging for proton therapy. *Br J Rad.*  
390 2020;93(1107):20190787.
- 391 9. Kalinichenko A, Lazurik VT, Zalyubovsky II. *Introduction to Radiation Acoustics*. Boca Raton:  
392 CRC Press; 2002.
- 393 10. Assmann W, Parodi K. The Sound of ions: acoustic detection of high-energy beams. *Nuclear*  
394 *Physics News*. *Nuclear Physics News*. 2020;30(1):20-24.
- 395 11. Hayakawa Y, Tada J, Arai N et al. Acoustic pulse generated in a patient during treatment by pulsed  
396 proton radiation beam. *Radiat Oncol Investig*. 1995;3(1):42-45.
- 397 12. Parodi K, Assmann W. Ionoacoustics: A new direct method for range verification. *Mod Phys Lett*  
398 *A*. 2015;30(17).
- 399 13. Sulak L, Armstrong T, Baranger H et al. Experimental studies of the acoustic signature of proton  
400 beams traversing fluid media. *Nucl Instrum Methods*. 1979;161(2):203-217.
- 401 14. Patch SK, Santiago-Gonzalez D, Mustapha B. Thermoacoustic range verification in the presence of  
402 acoustic heterogeneity and soundspeed errors - Robustness relative to ultrasound image of  
403 underlying anatomy. *Med Phys*. 2019;46(1):318-327.
- 404 15. Hayakawa Y, Tada J, Inada T, Kitagawa T, Wagai T, Yosioka K. Acoustic pulse generation in  
405 excised muscle by pulsed proton beam irradiation and the possibility of clinical application to  
406 radiation therapy. *J Acoust Soc Jpn (E)*. 1988;9(5):255-257.
- 407 16. Hayakawa Y, Tada J, Inada T, Wagai T, Yosioka K. Acoustic pulse generation in water by pulsed  
408 proton beam irradiation and its possible application to radiation therapy. *Jpn J Appl Phys*.  
409 1989;28(S1):217-219.
- 410 17. Tada J, Hayakawa Y, Hosono K, Inada T. Time resolved properties of acoustic pulses generated in  
411 water and in soft tissue by pulsed proton beam irradiation—a possibility of doses distribution  
412 monitoring in proton radiation therapy. *Med Phys*. 1991;18(6):1100-1104.
- 413 18. Assmann W, Kellnberger S, Reinhardt S et al. Ionoacoustic characterization of the proton Bragg  
414 peak with submillimeter accuracy. *Med Phys*. 2015;42(2):567-574.

- 415 19. Patch SK, Kireeff Covo M, Jackson A, et al. Thermoacoustic range verification using a clinical  
416 ultrasound array provides perfectly co-registered overlay of the Bragg peak onto an ultrasound  
417 image. *Phys Med Biol.* 2016;61(15):5621-38.
- 418 20. Haffa D, Yang R, Bin J et al. I-BEAT: ultrasonic method for online measurement of the energy  
419 distribution of a single ion bunch. *Sci Rep.* 2019;9(1):6714.
- 420 21. Jones KC, Vander Stappen F, Bawiec CR et al. Experimental observation of acoustic emissions  
421 generated by a pulsed proton beam from a hospital-based clinical cyclotron. *Med Phys.*  
422 2015;42(12):7090-7097.
- 423 22. Jones KC, Vander Stappen F, Sehgal CM, Avery S. Acoustic time-of-flight for proton range  
424 verification in water. *Med Phys.* 2016;43(9):5213-5224.
- 425 23. Lehrack S, Assmann W, Bertrand D et al. Submillimeter ionoacoustic range determination for  
426 protons in water at a clinical synchrocyclotron. *Phys Med Biol.* 2017;62(17):L20-L30.
- 427 24. Patch SK, Nguyen C, Dominguez-Ramirez D, et al. Thermoacoustic Range Verification During  
428 Pencil Beam Delivery of a Clinical Plan to an Abdominal Imaging Phantom. *Radiother Oncol.*  
429 2021;S0167-8140(21):06164-8.
- 430 25. Keil, E., Sessler, A. M. & Trbojevic, D. Hadron cancer therapy complex using nonscaling fixed  
431 field alternating gradient accelerator and gantry design. *Phys. Rev. ST Accel. Beams* 10, 054701  
432 (2007).
- 433 26. Garland JM, Appleby RB, Owen H, et al. Normal-conducting scaling fixed field alternating  
434 gradient accelerator for proton therapy. *Phys. Rev. ST Accel. Beams.* 2015;18(9), 094701.
- 435 27. Smith AR. Vision 20/20: proton therapy. *Med Phys.* 2009;36(2):556-68.
- 436 28. Ishi Y et al. Status report on FFAG accelerator complex at KURRI. *Proc of the 12th Annual*  
437 *Meeting of Particle Accel. Soc. of Japan; vols 368-370; 2015.*
- 438 29. Kuriyama Y et al. Status and development of a proton FFAG accelerator at KURRI for ADSR  
439 study. *Proc Of 2011 Particle Accelerator Conference, THP027; 2011:2172-2174.*
- 440 30. Ozoemelam I, van der Graaf E, van Goethem MJ, et al. Feasibility of quasi-prompt PET-based  
441 range verification in proton therapy. *Phys Med Biol.* 2020;65(24):245013.
- 442 31. Wang LV, Wu H-I. *Biomedical Optics: Principles and Imaging.* New York: Wiley; 2007.

- 443 32. Treeby, B. E. & Cox, B. T., Artin. k-Wave: MATLAB toolbox for the simulation and  
444 reconstruction of photoacoustic wave fields. *J Biomed Opt.* 2010;15:1117/1.3360308, DOI: doi  
445 PubMed: 02131410.
- 446 33. Allison J, Amako K, Apostolakis J et al. Recent developments in GEANT4. *Nucl Instrum*  
447 *Methods A.* 2016;835:186-225.
- 448 34. Kudo N, Zhang X, Yamamoto K. Measurement of the Wall thickness of the carotid artery using  
449 ultrasound radiofrequency Echo signals. *J Med Ultrason.* 1998;25(3):1-12.
- 450 35. Hayakawa used the short-pulsed proton beam (FWHM of 118 ns) from KEK synchrocyclotron  
451 and obtained 24 Pa per 1 Gy BP dose, but the position of the hydrophone was not available from  
452 the reference.
- 453 36. Takayanagi T, Uesaka T, Nakamura Y, et al. On-line range verification for proton beam therapy  
454 using spherical ionoacoustic waves with resonant frequency. *Sci Rep.* 2020; 10(1), 1-10.
- 455 37. Abe K, Arakawa M, Kanai H. Estimation method for sound velocity distribution for  
456 high-resolution ultrasonic tomographic imaging. *J Med Ultrason.* 2019;46(1):27-33.
- 457 38. Sanabria SJ, Ozkan E, Rominger M, et al. Spatial domain reconstruction for imaging  
458 speed-of-sound with pulse-echo ultrasound: simulation and in vivo study. *Phys Med Biol.*  
459 2018;63(21):215015.
- 460 39. Alsanea F, Moskvina V, Stantz KM. Feasibility of RACT for 3D dose measurement and range  
461 verification in a water phantom. *Med Phys.* 2015;42(2):937-46.
- 462 40. Yu Y, Li Z, Zhang D, et al. Simulation studies of time reversal-based photoacoustic  
463 reconstruction for range and dose verification in proton therapy. *Med Phys.*  
464 2019;46(8):3649-3662.
- 465 41. Freijo C, Herraiz JL, Sanchez-Parcerisa D, Udias JM. Dictionary-based photoacoustic dose map  
466 imaging for proton range verification. *Photoacoustics.* 2021;21:100240.
- 467 42. Matsuura T, Fujii Y, Takao S, et al. Development and evaluation of a short-range applicator for  
468 treating superficial moving tumors with respiratory-gated spot-scanning proton therapy using  
469 real-time image guidance. *Phys Med Biol.* 2016;61(4):1515-1531.
- 470 43. Kipergil EA, Erkol H, Kaya S, Gulsen G, Unlu MB. An analysis of beam parameters on  
471 proton-acoustic waves through an analytic approach. *Phys Med Biol.* 2017;62(12):4694-4710.

472

473

474 **Figure captions**

475

476 **Figure 1.** (A) Experimental setup. Proton beam accelerated by the FFA is incident on the water  
477 phantom, crossing the acrylic wall. A scintillator is set at the exit of the beam duct and it  
478 indirectly measures the beam pulse shape. A hydrophone is positioned 20 mm downstream of  
479 the beam range, facing this beam. (B) The signal measured by the scintillator and the Gaussian  
480 fitting curve.

481

482 **Figure 2.** (a) Bragg curve and (b, c) lateral beam profiles obtained by the Bragg peak ionization  
483 chamber and radiographic films, respectively. In (a), the solid curve shows the results obtained  
484 using Monte Carlo simulations.

485

486 **Figure 3.** Schematic representation of the wave propagation implied in TOF metrics to estimate  
487 the beam range. (a) Direct  $\gamma$ -wave from the BP, (c) the  $\gamma$ -wave reflected at the acrylic wall-water  
488 boundary, and (d) the  $\gamma$ -wave reflected at the boundary between the acrylic wall and the air.  
489 Because of the higher acoustic impedance of acryl compared to water and air, the resonance is  
490 formed in the acrylic wall. The resonance frequency of the wavelet (b), emitted from the wall,  
491 allowed to derive the sound speed in the acryl.

492

493 **Figure 4.** The time domain waveforms observed in the experiment (upper left) and the  
494 simulation (upper right), with the enlarged figures around wavelet (a) (lower left) and wavelets  
495 (c) and (d) (lower right). The red curves represent the simulation. In the lower figures, the  
496 simulation plot is shifted to match measured results for easing comparison. The thick arrows  
497 show the peaks selected for TOF or relative TOF metrics. The thin arrows refer to the peaks that  
498 were not used for TOF metrics.

499

500 **Figure 5.** Frequency spectrum of the waveforms shown in Figure 4, representing the experiment  
501 (black) and simulation (red). Frequency spectra of wavelet (a) (solid curves) and wavelets (c)  
502 and (d) (dashed curves) are shown in the right panel.

503

504 **Figure 6.** Schematic figure of the geometries considered in a simplified model in which the  
505 Bragg peak is assumed as a one-dimensional finite length heat source lying on the  $z$ -axis.

506 (a) Homogeneous medium (b) Layer structure consisting of air, acrylic wall, and water

507



508 **Tables**

509

510 **Table 1.** Acoustic properties of water, acryl, and air.

	$\rho(\text{kg/m}^3)$	$\beta(\text{K}^{-1})$	$v(\text{m/s})$	$C_p(\text{J/K/kg})$	$\Gamma$	$Z(\text{Ns/m}^3)$
Water (22°C)	1000	$2.06 \times 10^{-4}$	1488	4180	0.11	$1.56 \times 10^6$
Acryl	1180	$2.10 \times 10^{-4}$	2930	1400	1.29	$3.46 \times 10^6$
Air	1.293	$3.66 \times 10^{-3}$	340	1006	0.42	$4.40 \times 10^2$

511  $\rho$ : mass density,  $\beta$ : coefficient of volumetric thermal expansion,  $v$ : speed of sound,  $C_p$ : heat

512 capacity at constant pressure,  $\Gamma$ : Gruneisen coefficient, and  $Z$ : acoustic impedance.

513

514

515 **Table 2.** Relative and absolute TOF of the wavelets (c) and (d) and of the wavelet (a),  
 516 respectively, and the beam range estimated with these distinct metrics, both from the experiment  
 517 (upper row) and simulation (lower row). The values are the mean and SE of 100 independent  
 518 measurements (each consisting of 50 events).

		$\tau_n^{(c)} - \tau_n^{(a)}$	$\tau_p^{(d)} - \tau_n^{(a)}$	$\tau_p^{(a)}$
Experiment	Time ( $\mu$ s)	$89.47 \pm 0.02$	$96.27 \pm 0.01$	$13.98 \pm 0.01$
$R_{BPC} = 77.6$ mm	Range (mm)	$78.16 \pm 0.01$	$78.15 \pm 0.01$	$75.80 \pm 0.01$
Simulation	Time ( $\mu$ s)	85.98	92.74	13.42
$R_{sim} = 76.3$ mm	Range (mm)	75.57	75.52	76.63

519

520

521

522 **Table 3.** The water equivalent thickness of the additional acrylic plates (actual thickness  $\times$   
523 1.16) and the shift in the BP positions (mean  $\pm$  SE), estimated from the variation in the two  
524 metrics  $\tau_n^{(c)} - \tau_n^{(a)}$  and  $\tau_p^{(d)} - \tau_n^{(a)}$  from those obtained without the acrylic plates.

Thickness of additional acrylic plates (mmWEL)	$\Delta(\tau_n^{(c)} - \tau_n^{(a)})$ (mmWEL)	$\Delta(\tau_p^{(d)} - \tau_n^{(a)})$ (mmWEL)
4.6	$4.8 \pm 0.03$	$4.6 \pm 0.03$
9.3	$9.2 \pm 0.03$	$9.5 \pm 0.03$
13.9	$14.1 \pm 0.04$	$14.1 \pm 0.03$
18.6	$18.6 \pm 0.04$	$18.5 \pm 0.02$
23.2	$23.3 \pm 0.04$	$23.3 \pm 0.03$

525

526

527

528 **Table 4.** List of the absolute pressure values in ionoacoustics that can be retrieved from  
 529 previous research.

	Energy [MeV]	Pulse duration (FWHM) [μs]	Gy/pulse	Pressure, detector position (distance from the BP)	Expected pressure at 5 cm from the BP	Expected pressure per 1 Gy at 5 cm from the BP
cyclotron <sup>22</sup>	190	15-19	0.034	5.2 mPa <sup>*a</sup> , 5 cm	29 mPa	0.85 Pa
synchrocyclotron <sup>23</sup>	145–227	2.5-3.7	0.01	58 mPa <sup>*b</sup> , 5–10 cm	58–116 mPa <sup>*c</sup>	5.8–11.6 Pa <sup>*c</sup>
cyclotron <sup>19</sup>	50	1.76	2	11 Pa, 6.5 mm	1.4 Pa <sup>*c</sup>	0.72 Pa <sup>*c</sup>
FFA	100	0.047	0.35	7.5 Pa, 2 cm	3 Pa <sup>*c</sup>	8.6 Pa <sup>*c</sup>

530 <sup>\*a</sup> This value is per 6.1 mGy according to the ref.<sup>21</sup> <sup>\*b</sup> The maximum pressure amplitude of about 23  
 531 mV (Fig. 1 in ref.<sup>23</sup>) was converted to the pressure using the detector sensitivity (−168 (dB, re 1 V  
 532 μPa<sup>−1</sup>)) and the amplifiers (40 dB). <sup>\*c</sup>These values were roughly estimated assuming that the  
 533 pressure size is inversely proportional to the distance from the BP. <sup>22</sup>

534

535

536

537 **Table 5.** The maximum variation of the detected range (in mm) among 100 measurements,

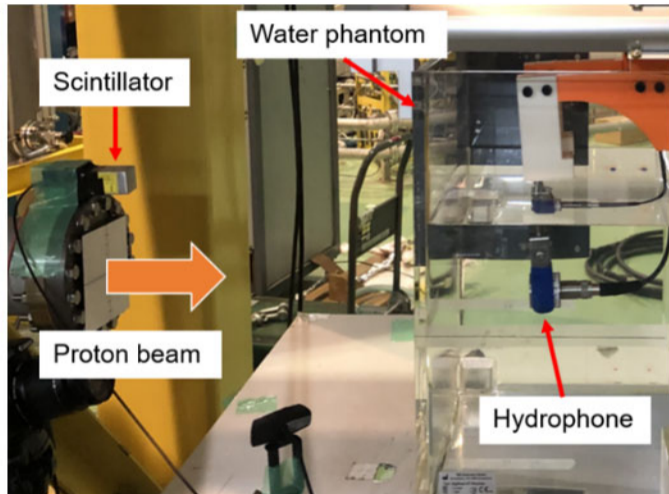
538 with numerous measurement averages.

Number of averages	Total dose [Gy]	Time used for range detection		
		$\tau_n^{(c)} - \tau_n^{(a)}$	$\tau_p^{(d)} - \tau_n^{(a)}$	$\tau_p^{(a)}$
1	0.35	10.8	13.3	2.1
5	1.75	4.8	1.1	0.7
10	3.5	3.1	0.7	0.6
50	17.5	0.7	0.5	0.4

539

540

(A)



(B)

